Interim Report   **IR-01-017**

Effects of Land Cover Change on Regional Atmospheric Chemistry and Climate in China

Allison Steiner (allison@eas.gatech.edu)

Approved by

Günther Fischer
Leader, Land Use Change Project

March, 2001

Contents

Abstract

The terrestrial biosphere can significantly affect the exchange of water and energy at the biosphere-atmosphere interface. Additionally, the land cover type can affect regional atmospheric chemistry and climate via biogenic volatile organic carbon (VOC) emissions and their formation of secondary organic aerosols. The broad goal of this study is to investigate the impact of land cover and vegetation changes on these specific chemistry and climate effects. The Common Land Model (CLM) is used to parameterize the biosphere-atmosphere interface over the Shanghai region in China. Phase I of this study, described in this report, generates input parameters for this model based on a time series of actual and derived parameters. Atmospheric forcing data are generated on an hourly temporal resolution based on a 20-year series of monthly and daily averages. Surface data, including land cover/land use and soil information, are generated for two scenarios: a) the current land cover and b) a "natural" land cover data set, derived to represent the absence of anthropogenic influences. Phase II of this study will evaluate the model sensitivity to these different input parameters. The potential impacts of land cover change on the regional atmospheric chemistry and climate using these two scenarios will be addressed.

Acknowledgments

About the Author

Allison Steiner began her Ph.D. program in September 1997, concentrating in Atmospheric Chemistry at the School of Earth and Atmospheric Sciences, Georgia Institute of Technology in Atlanta, Georgia, USA. Her main focus of research is biogenic volatile organic compound (VOC) emissions, their impacts on chemistry and climate, and the consequences of land cover change on these emissions. Her anticipated graduation date is May 2002.

Effects of Land Cover Change on Regional Atmospheric Chemistry and Climate in China

Allison Steiner

Introduction

The interaction between the biosphere and atmosphere is an important interface in climate models as it represents the lower boundary condition of the atmosphere [*Garratt*, 1993]. The description of this boundary condition can significantly impact the input and output of mass, momentum and energy into the atmosphere. Land surface parameterizations are usually included as a subroutine in large climate models to describe this interface and have been subject to several generations of development over the past few decades [*Sellers, et al.*, 1997]. The biosphere-atmosphere interface is also linked to atmospheric chemistry through the emissions of biogenic volatile organic compounds (VOCs), which are released from various forms of vegetation into the troposphere. These biogenic VOCs can have a significant impact on regional atmospheric chemistry by potentially amplifying the production of ground-level ozone, even in urban areas if sufficient NO_x is present [*NRC*, 1991; *Chameides et al.*, 1988; *Fehsenfeld et al.*, 1992]. Additionally, these compounds can be oxidized by free radicals in the atmosphere (e.g., the hydroxyl radical, the nitrate radical, or ozone) to form secondary organic aerosol (SOA) [*Hoffman et al.*, 1997; *Griffin et al.*, 1999a,b]. The addition of these aerosols to the atmosphere can impact incident radiation, thereby affecting the energy balance at the surface.

1.   Processing of Meteorological and Surface Parameters for Input into a Land Surface Parameterization

The broad focus of this study is to investigate the effects of biogenic VOC emissions and subsequent aerosols on regional chemistry and climate. The feedbacks between

these systems will be evaluated by coupling a land surface parameterization to a regional chemistry-climate model. A new land surface parameterization, the Common Land Model (CLM) [*Dai et al.*, 2001, in press], will represent the biosphere-atmosphere interface and will be coupled with the RegChemCM, a regional chemistry-climate model developed as a combination of the Regional Climate Model (RegCM) [*Giorgi et al.*, 1993a,b] and the Regional Acid Deposition Model (RADM)[*Chang et al.*, 1987]. The community-developed CLM is a compilation of several existing land surface parameterizations and is believed to provide a significant improvement over existing land surface parameterizations [*Zeng et al.*, 2000, in press]. This investigation will provide an unique ability to couple the emissions from vegetation with the regional chemistry-climate model, allowing a direct evaluation of how biogenic VOC emissions can impact both chemistry and climate.

Phase I includes the generation of the meteorological and surface input files required by the CLM. Phase II will evaluate the model's sensitivity to different meteorological and surface parameters. These investigations will be run offline, or uncoupled, from the regional chemistry-climate model. Additionally, the meteorological file generated in Phase I will be compared with simulated meteorological parameters from the RegCM. Also, it will allow the investigation of different input parameters to determine when finer spatial and/or temporal resolution may or may not be necessary. Another aspect of Phase II is to investigate the importance of subgrid land surface heterogeneity and its significance in the estimation of biogenic VOCs and aerosols. The CLM has the added advantage of evaluating several types of land surface within a model grid cell. This approach, developed by *Koster and Suarez* [1992], uses a mosaic structure that allows up to five "tiles" per model grid cell and conducts separate energy and water balances on each "tile."

The area of interest is a selected portion of the climate-chemistry model grid used in the ChinaMAP project, a study focused on the impacts of anthropogenic pollution on crop yields. The area is centered over the city of Shanghai and includes surrounding regions, specifically the wheat growing areas to the northwest and rice-growing regions to the southeast. The selected subset is twelve by twelve grid cells, covering an area of approximately 518,400 square kilometers, with a spatial resolution of 60km.

2. Required Parameters

2.1 Meteorological Forcing Data

Eight meteorological parameters are required to define the atmospheric input conditions for the CLM. These parameters are 1) incoming shortwave radiation, 2) incoming longwave radiation, 3) precipitation, 4) temperature, 5) the east-west wind component (u-wind), 6) the north-south wind component (v-wind), 7) the surface pressure, and 8) the specific humidity.

Typically, these parameters are generated at each time step by the coupled chemistry-climate model. The atmospheric parameters are used to force the land surface model, and the resulting surface fluxes are used to force the atmosphere at the next time interval. Twenty years (1960-1980) of meteorological data on an hourly temporal resolution are generated for use the CLM, as spinup time is required for the conditions to equilibrate. Analyses in Phase II will utilize the last two years of data.

2.2 Surface Data

Two different types of surface information are required for use within the CLM; land cover/land use information and soil description. The land cover/land use information defines the type of vegetation (e.g., deciduous or evergreen) or land use (e.g., urban or agricultural) and assigns associated ecological characteristics (e.g., leaf area index) and radiative transfer properties (e.g. aerodynamic roughness length, albedo) to each land cover/land use category. The classification system implemented for the land cover/land use categories is the International Geosphere Biosphere Programme (IGBP) system, which consists of seventeen categories (see Table 1). Additionally, the CLM has the capability to divide individual grid cells into fractions, allowing land surface heterogeneities to be included. Other parameters related to the land cover/land use information include fractional coverage of vegetation.

The soil description includes the soil color and the soil texture. The soil color is used to estimate the albedo, or reflectivity of radiation from the surface. Albedos are assigned to soil colors depending upon the moisture content of the soil and the wavelength of radiation (greater or less than 0.7 μm). The soil texture (or combination of percentages

of sand, silt and clay) is used to determine the thermal and hydrologic soil properties, which affect water transport.

3.   Data Collection and Methodology

3.1   Meteorological Data

Four sources of raw data were utilized for the meteorological input data:

1.   180-station Daily Precipitation Data [*Kaiser et al.*, 1993],

2.   65-station Monthly Meteorological Data [*Shiyan et al.*, 1997],

3.   5-kilometer Monthly Temperature Average Data, IIASA [*Prieler*, 1999], and

4.   Monthly diurnal temperature range averaged over 30 years [*New et al.*, 1999].

Daily precipitation and monthly surface pressures were utilized from the 180-station and 65-station databases, respectively. The following 65-station parameters were used to derive other required input parameters: relative humidity, mean wind speed, dominant wind direction, and cloud cover. Specific humidity is calculated from relative humidity and pressure measurements. The u- and v- wind components are calculated from the mean wind speed and dominant wind direction. Incoming short-and longwave radiations are calculated based on a simple parameterization described below and 65-station observational cloud cover and dewpoint temperature. Temperature is calculated from the monthly average temperature (the IIASA dataset) and the monthly average diurnal temperature range.

Meteorological station data was assigned to each model grid cell based on proximity. The proximity tool in ESRI's ArcView software was used to determine the station with the least distance to each model grid cell. Two different proximity analyses were performed for the 180-station precipitation data (see Figure 2) and the 65-station meteorological data (see Figure 3). After the proximity analysis was performed, the station data parameter was assigned to the model grid cell.

3.1.1 Shortwave Radiation

Shortwave radiation was calculated based on a parameterization described in *Iqbal* [1983] and *Dingman* [1994], due to the lack of sufficient solar radiation measurements

in China at the appropriate spatial and temporal resolutions. Because an hourly temporal resolution was required, the available monthly averages were not sufficient to accurately portray the diurnal variation in solar radiation.

Incident shortwave radiation comprises three components that are a function of the radiation reaching the top of the atmosphere: diffuse, direct, and backscattered. The clear-sky radiation reaching the top of the atmosphere (r_{toa}) is calculated as a function of the solar constant, the distance of the Earth from the Sun, and the latitudinal position on the Earth's surface:

$$r_{toa} = S E_o \cos\theta \qquad (1)$$

The solar constant, S, is defined as the irradiance reaching the top of the atmosphere and is approximately 1367 W m^{-2}. The eccentricity correction factor, E_o, corrects for the variable distance between the Earth and the Sun and is a function of the Julian day of the year. The zenith angle, θ, describes the angle between the local vertical and the angle of the sun's incoming beam. When the sun is directly overhead, the zenith angle is zero. The zenith angle is calculated as a function of the latitude and the declination angle, or tilt, of the sun.

The direct component of radiation, r_{dir}, estimates the amount of radiation reaching the surface of the Earth after interaction with particles in the atmosphere. It is the clear-sky top of atmosphere radiation (W m^{-2}) multiplied by the atmospheric transmissivity:

$$r_{dir} = r_{toa}\, \tau \qquad (2)$$

The atmospheric transmissivity, τ, represents the fraction of radiation passing to the surface after absorption or scattering and is parameterized as:

$$\tau = \tau_{sa} - \gamma_{dust} \qquad (3)$$

The first term, τ_{sa}, represents the fraction of radiation that is transmitted through the atmosphere after scattering and absorption by water vapor and other atmospheric gases, and the second term, γ_{dust}, represents the attenuation (or loss of energy) by interaction with dust. For the purposes of this study and the high uncertainty with this parameter, it is assumed that γ_{dust} equals zero. The parameter τ_{sa} is a function of the water vapor

content of the atmosphere and the path length of the solar radiation, and is parameterized as a modified form of Beer's Law [*Dingman*, 1994]:

$$\tau_{sa} = \exp(a + b\, M_{opt}) \qquad (4)$$

where a and b describe the effects of water vapor as a function of precipitable water and M_{opt} is the optical path length. These can be empirically described as:

$$a = -0.124 - 0.0207 W_p \qquad (5)$$

$$b = -0.0682 - 0.0248 W_p \qquad (6)$$

The precipitable water content is defined as the depth of water (in cm) that would be formed if all the water vapor were condensed to precipitation and is a function of the dewpoint temperature (in degrees C) [*Bolsenga*, 1964]:

$$W_p = 1.12 \exp(0.0614 T_d) \qquad (7)$$

The dewpoint temperature used for this calculation was based on a monthly average of the 65-station dewpoint temperatures. Monthly values were assumed to be constant over the daily and hourly variations. The dimensionless optical path length, M_{opt}, can also be empirically described as a function of the solar zenith angle, θ [*Kasten and Young, 1989*]:

$$M_{opt} = \frac{1}{(\cos\theta + 0.50572(96.07995 - \theta))^{-1.6364}} \qquad (8)$$

The diffuse component of radiation, r_{dif}, is also a function of the incoming clear-sky top of atmosphere radiation. It has been estimated that approximately half of the scattered direct beam reaches the surface of the Earth as diffuse radiation (r_{dif}) [*Dingman*, 1994], leading to the following parameterization:

$$r_{dif} = 0.5\, \gamma_s\, r_{toa} \qquad (9)$$

where γ_s is a term that accounts for the amount of radiation scattered by atmospheric gases and dust:

$$\gamma_s = 1 - \tau_s + \gamma_{dust} \qquad (10)$$

This term is derived from the definition of radiant energy balance, which states all energy must be partitioned between the fraction of radiation attenuated (i.e., absorbed, reflected and/or scattered (γ_s)), and the amount transmitted (τ), and these fractions must add to unity [*Campbell and Norman*, 1998]. The transmittance term (τ_s) is calculated in the same manner as the direct transmittance term (τ_{sa}, see equation 4), with variables a and b defined as:

$$a = -0.0363 - 0.0084 W_p \tag{11}$$

$$b = -0.0572 - 0.0173 W_p \tag{12}$$

Precipitable water (W_p) and optical path length (M_{opt}) for the diffuse case are calculated as in the direct case (equations 7 and 8).

The third component, the backscattered component, accounts for the reflection of radiation from the surface of the Earth. Approximately half of this reflected radiation is re-scattered back towards the Earth's surface. The backscattered radiation is a function of the global radiation (direct plus diffuse components), the surface albedo a, and the attenuation term γ_s as in the diffuse case:

$$r_{bs} = 0.5\, a\, \gamma_s\, (r_{dir} + r_{dif}) \tag{13}$$

The total radiation received at the surface under clear-sky conditions is the sum of these three components (direct, diffuse, and backscattered). Under cloudy skies, the amount of incoming shortwave radiation is reduced. The parameterization of this process is quite complicated and has been grossly simplified in this study to provide a simple approximation of the impact of clouds. An approximation by *Crowley* [1989] is used to reduced the amount of radiation due to cloudiness:

$$r_{sd} = [0.355 + 0.68(1 - N)](r_{dir} + r_{dif} + r_{bs}) \tag{14}$$

where N represents the cloud cover (as a fraction of one). Cloudiness data was derived from monthly 65-station data, where stations were assigned to individual model grid cells as described above and shown in Figure 3.

3.1.2 Longwave Radiation

Longwave radiation required an empirical solution due to the lack of direct observations, therefore a method developed by *Kimball et al.* [1982] was adopted and modified for the calculations. Longwave radiation, or radiation with wavelengths greater than approximately 4 μm, is emitted from atmospheric gases and clouds. In this study, it is calculated as a sum of two components: one longwave portion emitted from a clear-sky atmosphere and the second portion emitted from clouds.

The clear-sky atmospheric longwave emissions are based on a modified version of the Stefan-Boltzmann law:

$$l_{atm} = \varepsilon_a \, \sigma \, T_a^4 \tag{15}$$

where ε_a is the emissivity of the atmosphere, σ is the Stefan-Boltzmann constant (=5.67 x 10^{-8} W m^{-2} K^{-4}), T_a is the atmospheric temperature (K). The emissivity of the atmosphere is based on the atmospheric vapor pressure (e, in kPa) and air temperature (T_a, in K) at the surface level:

$$\varepsilon_a = 0.70 + 5.95 \times 10^{-4} \, e \, \exp(1500/T_a) \tag{16}$$

Atmospheric vapor pressure (e) is calculated from the saturation vapor pressure (Clausius-Clapyeron equation, see equation 30) and the relative humidity, derived from the 65-station dataset. Air temperatures are implemented from the IIASA database, (Prieler, 1999).

The second component of the longwave downward radiation is produced by the clouds, and it is assumed that this radiation emitted from this component is only transmitted through the atmosphere in the 8-14 μm window [*Idso*, 1981]. The transmissivity in this window, τ_8, is represented as:

$$\tau_8 = 1 - \varepsilon_8 \tag{17}$$

where ε_8 is the hemispherical emissivity of the atmosphere in the 8-14 μm window and is calculated from the zenith emittance, as defined by *Idso* [1981]:

$$\varepsilon_8 = \varepsilon_{8z}(1.4 - 0.4\varepsilon_{8z}) \tag{18}$$

$$\varepsilon_{8z} = 0.24 + 2.98 \times 10^{-6} \, e^2 \, \exp(3000/T_a) \qquad (19)$$

The fraction of the blackbody radiation emitted in the 8-14 μm window at a specific cloud temperature, T_c, is determined by [*Kimball et al., 1982*]:

$$f_8 = -0.6732 + 0.6240 \times 10^{-2} \, T_c - 0.9140 \times 10^{-5} \, T_c^2 \qquad (20)$$

The cloud temperature can be calculated as follows, assuming a temperature lapse rate of 0.01 K m^{-1} (*Loth et al.*, 1993]:

$$T_c = T_a - 1.23(T_a - T_d) \qquad (21)$$

where T_d is the dewpoint temperature in degrees K. The cloud component of the longwave downward radiation can then be calculated as:

$$l_{cld} = \tau_8 N \varepsilon_c f_8 \sigma T_c^4 \qquad (22)$$

where N is the fraction of cloud clover and σ is the Stefan-Boltzmann constant. Cloud cover fraction and dewpoint temperatures were based on monthly 65-station data observations. The total amount of longwave downward radiation is then equal to the sum of the two components:

$$r_{ld} = l_{atm} + l_{cld} \qquad (23)$$

3.1.3 Precipitation

Precipitation data was derived from the 180-station TR055 data, which provides daily precipitation data for 180 stations throughout China [*Kaiser et al.*, 1993]. A total of seventeen different stations were matched to the model grid cells for this analysis, as shown in Figure 2. Each model grid cell was assigned a precipitation station based on the nearest station location, performed by the proximity analysis tool in ESRI's ArcView software.

Daily precipitation totals were available for each station over the entire twenty-year time series (1960-1980). Hourly data values were calculated using an assumption about local precipitation events, as few studies have been performed on the diurnal variation of precipitation in China. Over the mainland areas, strong daytime heating often causes

afternoon convective events [*Zhang and Lin*, 1992]. Based on these observations, the daily precipitation totals were divided equally between four hours in the local afternoon.

Further sensitivity studies will be performed to evaluate the impact of different types of precipitation events on the land surface processes.

3.1.4 Temperature

Temperature data was compiled from a monthly-averaged temperature database of China prepared by IIASA [*Prieler, 1999*]. This dataset is a thirty-year time series (1958-1988) of monthly temperature averages developed from 265 meteorological station measurements, long-term averages of mean monthly temperature on a 5-km grid, and a digital elevation model.

The temperature data was processed for this study's region of interest using ArcView and ArcInfo software. Because the model grid cell resolution (60-km) is much coarser than the temperature data, the 5-km temperature data was intersected with each model grid cell. A mean temperature value for each 60-km model grid cell was estimated using the ArcInfo GRID command, ZONALMEAN. This calculates the mean temperature value based on all 5-km grid cells with each 60-km model grid cell.

This provided an average monthly temperature value for each model grid cell. It is assumed that each daily temperature is equal to the monthly mean temperature. To include additional temporal resolution, a diurnal temperature range was employed to show the fluctuation of temperature throughout the day. A time series of monthly diurnal temperature ranges was available from Climate Research Unit (CRU) 0.5 degree gridded monthly climate data, provided by the Climate Impact LINK Project [*New et al., 1999*]. An average monthly diurnal temperature range (based on the monthly averages from years 1961-1990) was used to provide a daily temperature variation. The 0.5-degree resolution diurnal temperature range was intersected with the model grid cells, allowing the assignment of a diurnal temperature range to each model grid cell.

This range was then used to calculate an hourly variation in temperature centered on the monthly average temperature for each model grid cell. A sinusoidal function was implemented to calculate the temperature, T_t, at each hour t:

$$T_t = \frac{dtr}{2}\sin\left(\frac{2\pi}{24}(t-locn)\right)+T_{ave} \qquad (24)$$

where *dtr* is the diurnal temperature range, *locn* is the horizontal shift to allow for the maximum temperature to occur at local noon (based on the longitude of the model grid cell), and T_{ave} is the monthly average temperature for the model grid cell. The use of this function allows a sinusoidal variation in temperature, with the maximum occurring two hours after local noon, based on observational daily maximum temperatures in China [*Zhang and Lin, 1992*].

3.1.5 u- and v-wind components

The u-wind component (or zonal east-west component) and the v-wind component (or meridional north-south component) were developed from eleven stations in the 65-station data set, as shown in Figure 3. Similar to the precipitation stations, a proximity analysis was performed to assign a meteorological station to each model grid cell.

The data set provided a monthly mean wind speed (m s^{-1}) and a dominant wind direction for the particular month. The wind speed was recorded using an EL electric wind direction and speed device and a Dines wind direction and speed recorder [*Shiyan et al., 1997*]. The monthly dominant wind direction is the most frequent wind direction observed during the month and is measured in sixteen directions. If the magnitude, *ws*, and the direction of the wind, *drx*, is known, the two components (zonal and meridional) can be calculated:

$$u = ws\,\sin(drx) \qquad (25)$$

$$v = ws\,\cos(drx) \qquad (26)$$

The monthly measured wind speeds were used for daily and hourly wind speeds, thereby assuming them to be constant throughout the month.

3.1.6 Surface Pressure

The surface pressure was derived from the 65-station database. The monthly surface pressure value, measured in millibars, was used for all daily and hourly values within that month. Fortin and Kew-pattern barometers and an aneroid barograph were utilized for these measurements [*Shiyan et al., 1997*].

11

3.1.7 Specific Humidity

The specific humidity, q_m, is the relative concentration of water vapor. It can also be defined as the ratio of the mass of water vapor (m_v) to the mass of total air, including m_v and the mass of dry air (m_d):

$$q_m = \frac{m_v}{m_d + m_v} \tag{27}$$

By substituting the Ideal Gas Law, this quantity can also be expressed by the following relationships, which relate the quantity as a function of pressure instead of mass, as pressure is more easily measured in the atmosphere:

$$q_m = \frac{MW_v}{MW_d} \frac{e}{p + e[MW_v/MW_d - 1]} \tag{28}$$

where MW_v is the molecular weight of water (=18 grams/mole), MW_d is the molecular weight of dry air (=29 grams/mole), p is the atmospheric pressure (mb), and e is the vapor pressure (mb). Generally, it can be assumed that the ambient pressure is much larger than the vapor pressure, reducing the above equation to:

$$q_m = \frac{MW_v}{MW_d} \frac{e}{p} \tag{29}$$

The quantity p is measured at the station location as described above and the vapor pressure, e, can be calculated based on the saturation vapor pressure and the relative humidity. The saturation vapor pressure is a function of temperature only and can be calculated from a form of the Clausius-Clapyeron equation:

$$e_s = 6.11 \exp\left[17.3 \frac{T_a - 273.15}{T_a - 273.15 + 237.3}\right] \tag{30}$$

where T_a is the ambient air temperature and e_s is in millibars. The vapor pressure, e, can be calculated from the saturation vapor pressure (e_s) and the relative humidity (RH) as follows:

$$e = e_s \frac{RH}{100} \tag{31}$$

Therefore, three observed meteorological parameters are required to perform the specific humidity calculation: the atmospheric surface pressure, the relative humidity,

and the air temperature. Surface pressure and relative humidity are available from the 65-station meteorological dataset as described above. The relative humidity was measured using a ventilated psychrometer and a hair hygrometer [*Shiyan et al.,* 1997]. Monthly measurements of the pressure and relative humidity were used for the specific humidity calculation; hourly values were assumed constant throughout the month. Temperature values were taken from the IIASA dataset [*Prieler, 1999*].

3.2   Surface Data

3.2.1   IGBP Land Cover/Land Use Classification

Land cover/land use classification data in the seventeen IGBP categories (see Table 1) were obtained from the EROS Data Center Distributed Active Archive Center (EDC DAAC) at a 1-km resolution [EDC DAAC, 2000]. This data set was derived from the Advanced Very High Resolution Radiometer (AVHRR) satellite from April 1992 through March 1993. The land cover is predominantly determined from satellite-derived normalized difference vegetation index (NDVI) composites supplemented by ancillary data including digital elevation data, ecoregion interpretations, country or regional-level vegetation and land cover maps [*Brown et al.*, 1993; *Loveland et al.*, 1991].

The data utilized from the website was the Eurasia data set in the Lambert Equal Area Azimuthal projection. The projection of the data was changed to the Lambert Conformal Conic projection to match the projection of the model grid domain. After the land cover data was in the proper projection, the ArcInfo GRID command COMBINE was used to intersect the land cover data with the model grid cells. This provides a data file that lists the count of the number of raster cells (or pixels) of a land cover category within each model grid cell. The data was processed in a database program to compute the area of each land cover category within each model grid cell. This data was then processed into a properly formatted file to be read as input for the CLM. The land cover for the region of interest is shown in Figure 4.

3.2.2   Soil Data

Soils data were obtained from the IIASA soils database for China, Mongolia and Russia [*FAO and IIASA, 1999*] and the T42 file used by the LSM [*Bonan*, 1996]. Soil texture

13

data was also available from the T42 data file, but at a much coarser resolution than the FAO soil database. The FAO soils data for the region of interest is shown in Figure 5.

The soil texture, or relative percentages of sand, silts, and clay, is required to estimate the infiltration of water into the soil in the land surface parameterization model. These parameters are particularly important in the water balance at the surface of the earth and can significantly impact the flux of water to the atmosphere. The soil texture was derived from the FAO soil code classification, soil information in the FAO soil legends, and the USDA Soil Taxonomy guide [FAO, 1978; USDA, 1998]. Typically, two methods were used to assign the soil texture to a particular soil type. The first method used the soil profiles present in the FAO legends, which listed general soil types at specified depths (e.g., loam, clayey loam, etc.). A soil texture triangle was used to assign component percentages based on these general soil types. If no soil profile was found for a particular FAO soil type, a mapping of the FAO soil categories to the USDA soil categories was performed based on the USDA Soil Taxonomy orders. A typic soil profile for the USDA soil orders based on field samples can be found in the Soil Taxonomy Guide [USDA, 1998], which provides typical soil properties, including percentages of sand, silt and clay. Table 2 lists the dominant FAO soil types present in the domain, the method used to determine the texture, as well as the component percentages for each category.

Several special cases arose when classifying the soil texture. The first was of the addition of a relatively new soil class in the FAO classification, the Leptosols (FAO Codes 1101 and 1103). Leptosols are defined as a weakly developed shallow soil, and little specific testing information was available for this new category. For this reason, the second most dominant soil in the model domain was used to determine the texture. This soil type was present in three different model grid cells, and the second most dominant soil depended on the location of these grid cells. Also, little specific information was available for the Alisols categories (FAO codes 2700 and 2701). The alisols typically have a nitic soil horizon within the first 100cm, and are characterized by being at least 30 percent clay, with a silt to clay ratio of less than 0.4. A soil texture of 50% clay, 15% silt, and 15% sand was assumed for this soil type.

The FAO soil database was provided as a polygon coverage, then was converted to a grid coverage and intersected with the model grid cells. The most dominant soil type in each grid cell was found using the Arc/Info GRID command ZONALMAJORITY. This method provided the dominant soil category within each model grid cell. This dominant soil category was used with the above-described method to determine the soil texture for each model grid cell.

The soil color was determined from the T42 Land Surface Model (LSM) dataset [*Bonan*, 1996], which provides soil data on a resolution of 2.8125 degrees latitude/longitude. In the future, it would be preferable to derive a soil color database developed on the finer resolution FAO soil data. However, this is the most accurate soil color data available at this time. The T42 global file was gridded from an ASCII file, then intersected with the model grid cell to determine the most dominant soil color within each model grid cell. This was also performed using the ZONALMAJORITY command.

4. Future and Proposed Research

The input data sets developed during Phase I of the project will be utilized to perform offline runs to investigate the impacts of biogenic emissions on regional chemistry and climate. As part of Phase II, several sensitivity tests will be performed to evaluate the importance of different meteorological parameters. The following sensitivity tests are proposed:

a. Base case runs performed with meteorological data as described in Section 3.0 above.

b. Model runs with simulated RegCM meteorological data.

c. Experiments with precipitation.

- Use weekly averaged precipitation instead of daily precipitation.
- Experiment with different types of precipitation events (e.g., split all precipitation equally between all hours, make precipitation only in morning instead of afternoon).

d. Experiments with temperature (e.g., eliminate diurnal temperature range, using monthly averaged temperature for all time steps).

e. Correlate cloud cover fraction to precipitation events.

f. Experiments with cloud effects (e.g., changing parameters of cloudiness).

Additional sensitivity tests can be performed with the surface data, including:

a. Using a historical land cover/land use dataset.

b. Altering the soil texture.

c. Determining a finer resolution soil color data set.

These tests will provide a better understanding of the importance of the input parameters for future studies with the land surface model. Phase II of the study, which involves coupling of the land model to the chemistry-climate model, will investigate the overall objectives as described in the introduction and will address the impact of land surface information and land cover changes on regional chemistry and climate.

References

Bolsenga, S.J., Daily sums of global radiation for cloudless skies, U.S. Army Cold Regions Research and Engineering Laboratory Research Report, Hanover, NH, 1964.

Bonan, G., A land surface model (LSM version 1.0) for ecological, hydrological and atmospheric studies: Technical description and user's guide, NCAR Technical Note, NCAR/TN-417+STR, 1996.

Brown, J.F., T.R. Loveland, J.W. Merchant, B.C. Reed, and D.O. Ohlen, Using multisource data in global land cover characterization: concepts, requirements and methods, *Photo. Eng. & Remote Sensing, 59*, 977-983, 1993.

Campbell, G.S. and J.M. Norman. *An Introduction to Environmental Biophysics, Second Edition*. Springer, New York, 1998.

Chameides, W.L., R.W. Lindsay, J. Richardson, and C.S. Kiang, The role of biogenic hydrocarbons in urban photochemical smog: Atlanta as a case study, *Science, 241*, 1473, 1988.

Chang, J.S., et al., A three-dimensional Eulerian acid deposition model: Physical concepts and formulation, *J. Geophys. Res.*, 92, 14,681-14,700, 1987.

Croley, T.E. II. Verifiable evaporation modeling on the Laurentian Great Lakes. *Water Resour. Res., 25*, 781-792, 1989.

Dai, Y., et al., The Common Land Model (CLM) version 1.0, *Bull. Amer. Meteor. Soc.*, submitted, 2001.

Dingman, S.L. *Physical Hydrology*. Prentice Hall, Upper Saddle River, NJ, 1994.

EDC DAAC, Earth resources observing system Data Center Distributed Active Archive Center, *http://edcwww.cr.usgs.gov/landdaac/glcc/glcc.html*.

FAO, Soil Map of the World, 1:5000000, Volume VIII North and Central Asia, FAO-Unesco, Paris, 1978.

FAO-IIASA, (CD-ROM) Soil and Physiographic Database for North and Central Eurasia, FAO, Rome 1999.

Fehsenfeld, F., et al., Emissions of volatile organic compounds from vegetation and their implications for atmospheric chemistry, *Global Biogeochem. Cycles, 6*, 389-430, 1992.

Garratt, J.R., Sensitivity of climate simulations to land-surface and atmospheric boundary layer treatments – a review, *J. Climate, 6*, 419-499, 1993.

Giorgi, F., M.R. Marinucci, and G.T. Bates, Development of a second generation regional climate model (RegCM2), Boundary-layer and radiative processes, *Mon. Weather Rev., 121*, 2794-2813, 1993.

Giorgi, F., M.R. Marinucci, G.T. Bates, and G. De Canio, Development of a second generation regional climate model (RegCM2), Convective processes and assimilation of lateral boundary conditions, *Mon. Weather Rev., 121*, 2814-2832, 1993b.

Griffin, R.J., D.R. Cocker III, R.C. Flagan, and J.H. Seinfeld, Organic aerosol formation from the oxidation of biogenic hydrocarbons, *J. Geophys. Res., 104*, 3555-3567, 1999a.

Griffin, R.J., D.R. Cocker III, and J.H. Seinfeld, Estimate of global atmospheric organic aerosol from oxidation of biogenic hydrocarbons, *Geophys. Res. Letts., 26*, 2721-2724, 1999b.

Hoffmann, T., J.R. Odum, F. Bowman, D. Collins, D. Klockow, R.C. Flagan, and J.H. Seinfeld, Formation of organic aerosols from the oxidation of biogenic hydrocarbons, *J. Atmos. Chem.*, 26, 189-222, 1997.

Idso, S.B. A set of equations for full spectrum and 8- to 14-μm and 10.5- to 12.5-μm thermal radiation from cloudless skies. *Water Resour. Res., 17*, 295-304, 1981.

Iqbal, M., *An Introduction to Solar Radiation*, Academic, San Diego, Calif., 1983.

Kaiser, D., S. Tao, C. Fu, Z. Zeng, Q. Zhang, W-C. Wang, and T. Karl, Climate Data Bases of the People's Republic of China 1841-1988. DOE/NBB-0091T, TR055, U.S. Department of Energy, Washington, D.C., 1993.

Kasten, F. and A.T. Young. Revised optical air mass tables and approximation formula. *Applied Optics, 28*, 4735-4738, 1989.

Kimball, B.A., S.B. Idso, and J.K. Aase. A model of thermal radiation from partly cloudy and overcast skies, *Water Resour. Res., 18*, 931-936, 1982.

Koster, R.D. and M.J. Suarez. Modeling the land surface boundary in climate models as a composite of independent vegetation stands. *J. Geophys. Res., 97*, 2697-2715, 1992.

Loth, B., H.F. Graf, and J.M Oberhuber. Snow cover model for global climate simulations. *J. Geophys. Res., 98*, 10,451-10,464, 1993.

Loveland, T.R., J.W. Merchant, D.O. Ohlen, and J.F. Brown. Development of a land-cover characteristics database for the coterminious U.S., *Photo. Eng. & Remote Sensing, 57*, 1453-1463, 1991.

National Research Council, *Rethinking the Ozone Problem in Urban and Regional Air Pollution*, National Academy of Sciences Press, 500 pp., 1991.

New, M., M. Hulme, and P. Jones. Representing twentieth-century space-time climate variability. Part I: Development of a 1961-90 mean monthly terrestrial climatology, *J. Climate, 12, 3*, 829-856, 1999.

Prieler, S. *Temperature and precipitation variability in China – A gridded monthly time series from 1958 to 1988.* IIASA Interim Report IR-99-074, International Institute for Applied Systems Analysis, Laxenburg, Austria, 1999.

Sellers, P.J., et al., Modeling the exchanges of energy, water, and carbon between continents and the atmosphere. *Science, 275,* 502-509, 1997.

Shiyan, T., F. Congbin, Z. Zhaomei, and Z. Qingyun, Two long-term instrumental climatic data bases of the People's Republic of China. ORNL/CDIAC-102, NDP-039/R1, Carbon Dioxide Information Analysis center, Oak Ridge National Laboratory, Oak Ridge, TN, 1997.

USDA, *Keys to Soil Taxonomy, Eighth Ed.*, 1998.

Zeng, X., M. Shaikh, Y. Dai, R.E. Dickinson, and R. Myneni, Coupling of Common Land model to the NCAR Community Climate Model, *J. Climate*, submitted, 2000.

Zhang, J. and Z.Lin, *Climate of China*. John Wiley & Sons, New York, 1992.

Table 1. International Geosphere-Biosphere Program Land Cover/Land Use Classification.

IGBP Category	Description
1	Evergreen Needleleaf Forest
2	Evergreen Broadleaf Forest
3	Deciduous Needleleaf Forest
4	Deciduous Broadleaf Forest
5	Mixed Forests
6	Closed Shrublands
7	Open Shrublands
8	Woody Savannas
9	Savannas
10	Grasslands
11	Permanent Wetlands
12	Croplands
13	Urban and Built-up
14	Cropland/Natural Vegetation Mosaic
15	Snow and Ice
16	Barren or Sparsely Vegetated
17	Water Bodies

Table 2. Determination of Soil Texture.
Note: Only dominant FAO soil categories are listed.

FAO Soil Category	FAO Code	Method	% Sand	% Silt	% Clay
Eutric Cambisols	503	Soil Taxonomy	5	40	55
Gleyic Cambisols	504	Soil Taxonomy	5	40	55
Eutric Fluvisols	602	FAO Index	20	40	40
Calceric Fluvisols	605	FAO Index	20	40	40
Mollic Fluvisols	606	Sim. to other Fluv.	20	40	40
Eutric Gleysols	702	FAO Index	70	15	15
Dystric Leptosols	1101	2 ° soil type			
Rendzic Leptosols	1103	2 ° soil type			
Haplic Solonchaks	1802	FAO Index	20	40	40
Haplic Luvisols	2401	Soil Taxonomy	28	12	60
Stagnic Luvisols	2407	Soil Taxonomy	28	12	60
Haplic Acrisols	2601	Soil Taxonomy	12	15	73
Alisols	2700	Soil Definition	50	15	35
Haplic Alisols	2701	Soil Definition	50	15	35

Figure 1.   Area of Interest. Subgrid denotes model grid cells included in this study.

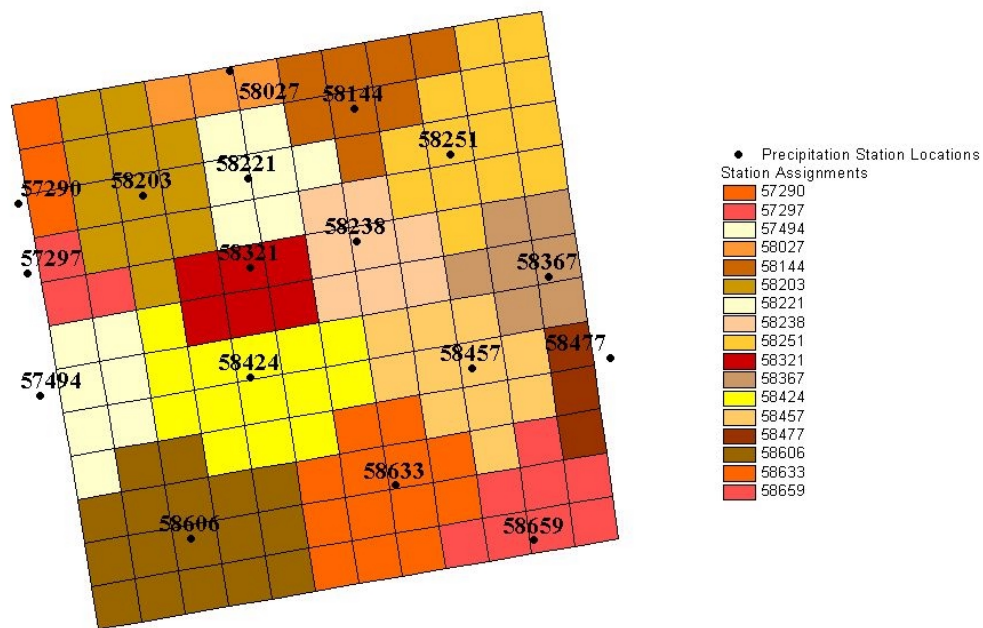**Figure 2.**   Precipitation station proximity analysis, based on 180-Station WMO dataset.
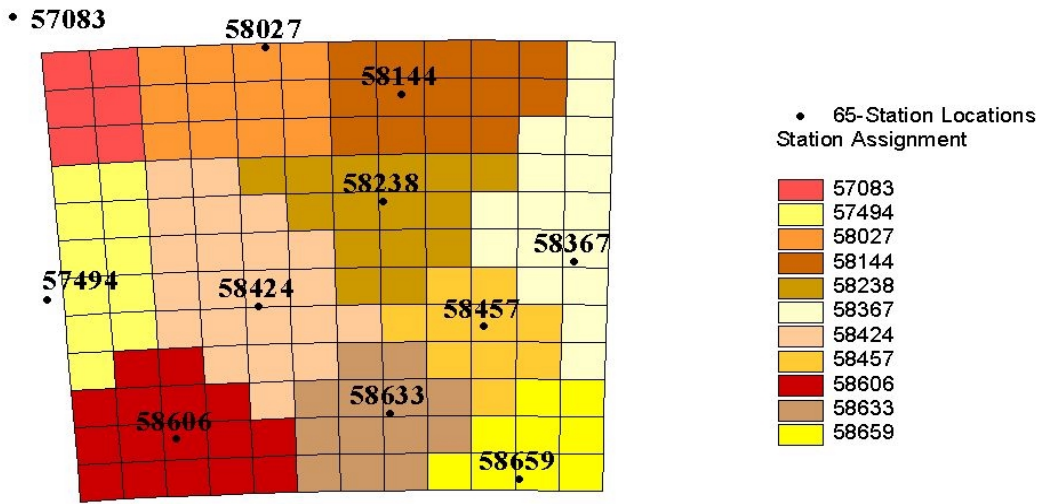Projection: Lambert Equal Area Azimuthal.

21

Figure 3. Meteorological station proximity analysis, based on 65-Station CAS dataset Projection: Geographic (distorted grid shape due to projection transformation).
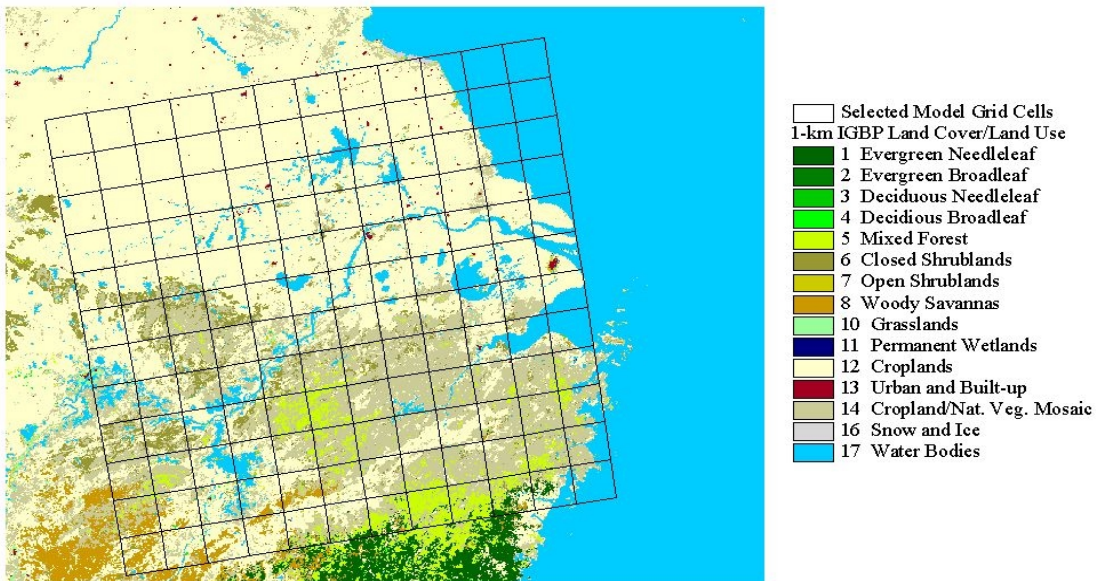

Figure 4. IGBP Land Cover/Land Use 1-km AVHRR Data. Projection: Lambert Equal-Area Azimuthal.
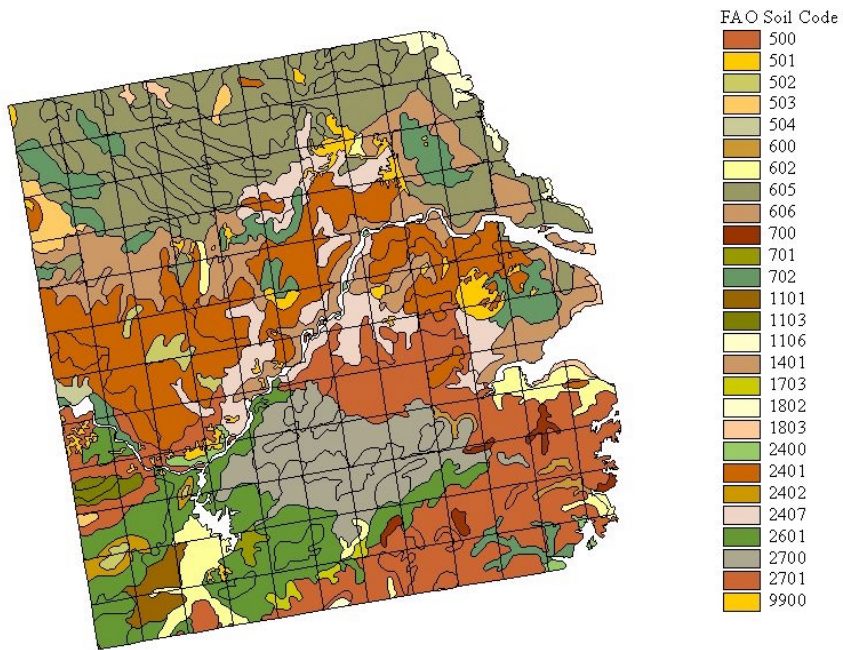
Figure 5.   Soil data categorized by FAO Soil Code.
Projection: Lambert Equal-Area Azimuthal.